Femtosecond Laser-Induced Simultaneous Surface Texturing and Crystallization of a-Si:H Thin Film: Absorption and Crystallinity

Hongliang Wang
Panjawat Kongsuwan
Gen Satoh
Y. Lawrence Yao

Department of Mechanical Engineering,
Columbia University,
New York, NY 10027

Hydrogenated amorphous silicon (a-Si:H) thin films have been considered for use in solar cell applications because of their significantly reduced cost. Their overall efficiency and stability, however, are less than that of their bulk crystalline counterparts. Limited work has been performed on solving the efficiency and stability issues of a-Si:H simultaneously. In this study, both surface texturing and crystallization on a-Si:H thin film are achieved through one-step femtosecond laser processing. The nanoscale conical and pillar-shaped spikes formed on the surface of a-Si:H films by femtosecond laser irradiation in both air and water are presented and enhanced light absorption is observed due to light trapping based on surface geometry changes, while the formation of a mixture of hydrogenated nanocrystalline silicon (nc-Si:H) and a-Si:H after crystallization suggests that the overall material stability can potentially be increased. The relationship among crystallinity, fluence, and scan speed is also discussed. Furthermore, a comparison of absorptance spectra for various surface morphologies is developed. Finally, the absorptance measurement across the solar spectrum shows that the combination of surface texturing and crystallization induced by femtosecond laser processing is very promising for a-Si:H thin film solar cell applications. [DOI: 10.1115/1.4006548]

1 Introduction

Many industrial solar cells in use today use bulk materials as absorbers with crystalline silicon being the most prevalent. However, crystalline silicon suffers from the disadvantage of high material cost since relatively large thicknesses are required primarily due to its low absorption coefficient. Recently, thin film absorbers are becoming more and more attractive based on their potential for low-cost modules, possibility to create tandem junctions, and large-scale manufacturability [1–3]. a-Si:H is the most popular material for use in thin film form due to its low energy economy (cost/watt). The main issue with a-Si:H is the high order of dangling bonds which act as recombination centers that severely reduce the carrier lifetime which results in the solar cell efficiency being below 10%. Additionally, this initial efficiency will decrease by 50% or more when exposed to sunlight over a period of months which is known as the Staebler–Wronski effect or SWE [4,5].

Surface texturing by laser processing is a way to improve efficiency, but the SWE remains. The most important material properties that play a role in the SWE are the high disorder in the Si network and high concentration of impurities, which cause some atoms to have dangling bonds that act as defects. Although these dangling bonds can be passivated by hydrogen, light exposure generates electron-hole pairs that will combine. The released energy can break the Si-H bond and promote H to a transport state. The diffusing H-atom successively breaks Si-Si bonds creating Si-H bonds and a neighboring dangling bond. This increasing defect density caused by the so-called SWE can further reduce the cell efficiency. In a thermal annealing process, the hydrogen atoms will revert back to their original positions. This process can reverse the SWE; however, the same degradation process will happen again when the material is exposed to sunlight [5,6]. In order to reduce the SWE, hybrid a-Si:H/nc-Si:H tandem modules have been developed and are able to achieve both higher efficiency and stability compared with single junction a-Si:H [7]. a-Si:H with reduced thickness will contain less defects, and the nanocrystalline silicon (nc-Si:H) is more stable and has wider spectral absorption compared to a-Si:H. To eliminate the need for two deposition steps, laser-induced crystallization of a-Si:H has been proposed to produce a mixture of nc-Si:H and a-Si:H and simultaneously form a light trapping texture on the surface of the material. Therefore, laser-based treatment of a-Si:H may solve the efficiency and stability issues in a one-step process, which is a promising methodology for thin film solar cell fabrication.

While both nanosecond and femtosecond pulsed lasers are useful tools for a-Si:H crystallization [8,9], the femtosecond laser-induced crystallization includes a nonthermal ultrafast phase transition, followed by a thermal process which is different from rapid thermal melting and resolidification caused by a nanosecond laser [10]. However, due to the much smaller thermal diffusion and heat-affected-zones, femtosecond laser processing is more desirable for texturing the limited thickness of thin films. Extensive work on surface texturing of crystalline bulk silicon had been reported by Mazur et al. [11,12]. Micron-size conical spikes have been generated on crystalline silicon a few hundred-micrometers thick when irradiated with a femtosecond laser in different background gases, such as SF_6, N_2, and air, and a significant enhancement in light absorptance is achieved after texturing. However, limited work is presented for a-Si:H thin films. Nayak et al. [13] showed the observation of crystallization and simultaneous formation of surface structures on roughly 2 μm-thick a-Si:H thin films through femtosecond laser processing in air and showed that the nanosizes spikes resulted in similar absorption enhancement to that of laser processed crystalline bulk silicon. However, the light absorption for different surface geometries on a-Si:H surfaces has

Contributed by the Manufacturing Engineering Division of ASME for publication in the Journal of Manufacturing Science and Engineering. Manuscript received November 4, 2010; final manuscript received March 27, 2012; published online May 4, 2012. Assoc. Editor: Yong Huang.

not been characterized after laser irradiation in different processing environments, such as background gases and water.

In the previous study [14–16], the formation of nanoscale conical and pillar-shaped spikes on a-Si:H surfaces has been studied through scanning electron microscopy (SEM) and atomic force microscopy (AFM) for femtosecond laser irradiation in both air and water. Base on the parametric study of the relationship between the surface morphologies and processing conditions, the dependence of light absorptance on typical surface structure is studied by spectrophotometry while the effect of laser processing on crystallinity is investigated by X-ray diffractometry (XRD). The combined effects of light trapping surface structure and crystallization on a-Si:H suggests a one-step process for potentially enhancing the efficiency and stability of thin film solar cells.

2 Background

2.1 Factors Affecting Light Absorption. The light absorption capabilities of a material depend on its optical properties (refractive index, absorption coefficient), film thickness, and surface roughness. This paper mainly focuses on a-Si:H, and thus, the optical properties are considered to be consistent between samples. As known, the thicker the film, the higher the light absorption. However, a thick a-Si:H layer increases the number of recombination centers. As a result, the stability performance deteriorates and the cost increases. Antireflection coating is also a way to improve absorption, but additional costs for the material and deposition process are also introduced. Therefore, changing the surface geometry is the most economical and efficient way for enhancing the light absorptance.

Yagi et al. [17] showed a significant reduction in the reflectance of crystalline silicon with a pyramidal textured surface by anisotropic etching and also found that the reflectance of silicon deposited on V-shaped glass substrates increases with increasing angle of the V-shape. Halbwax et al. [18] investigated the dependence of absorption on different shape surface structures and showed conical spikes had the best absorption, followed by pillars and pyramids. Hua et al. [19] showed the absorption caused by different surface geometries, and found that surface structures with higher density, smaller top angle, and a spike shape that can introduce a greater number of reflections within the periodic structures, will absorb a larger fraction of the incoming light.

2.2 Femtosecond Laser-induced Crystallization. During femtosecond laser irradiation, the conservation equation for electrons excited by multiphoton absorption can be written as [10]

$$\frac{\partial N(x,t)}{\partial t} = \frac{(1-R)\alpha I(x,t)}{h\nu} + \frac{(1-R)^2 \beta I^2(x,t)}{2h\nu} \tag{1}$$

where N is electron density, R is reflectivity, α is linear absorption coefficient, $h\nu$ is the photon energy of the laser beam, β is the two photon absorption coefficient, and $I(x,t)$ is the laser intensity expressed as follows [10]:

$$\frac{\partial I(x,t)}{\partial t} = -(\alpha + \Theta N) I \tag{2}$$

where Θ is the free carrier absorption cross section.

If the critical density of electrons, which is estimated to be 10^{22} cm^{-3} [10], is exceeded, they are excited out of the bonding states of the valence band into the conduction band, and a nonthermal ultrafast phase transition will occur. Due to the removal of a significant number of electrons from the material, the bond charge will be so weak that the material structure will no longer be stable and will collapse caused by the atoms' enhanced mobility. Thus, the phase changes to liquid without thermal effects [20,21]. This ultrafast phase transition caused by a high-density photo-excited plasma without increasing the materials thermal energy is called the plasma annealing mechanism. Van Vechten et al. [20] showed that, as the plasma becomes less dense due to expansion and energy transfer to the material, the material will pass back through the phase transition and covalent bonding will gradually reappear. Crystallization of the material can occur if this solidification process does not occur too quickly. Choi et al. [10] considered that the nonthermally melted layer vanishes in a few picoseconds during which time a portion of the covalent bonds start to reappear due to relaxation of electrons back to the valence band. Within a nanosecond, the surface starts to be melted due to thermal diffusion after the transfer of energy from the excited electrons to the material. Resolidification of this thermal melting layer causes the final crystallization. Callan et al. [22] also suggests that the ultrafast nonthermal phase transition described above does not lead to a thermodynamically stable crystalline phase, but to a nonequilibrium disordered phase, and this disorder-to-disorder phase transition can cause defect formation which is considered to be the driving force for subsequent rapid nucleation [10]. This process which includes nonthermal and thermal melting leading to solidification describes femtosecond laser-induced crystallization, which is different from nanosecond laser crystallization where only a rapid thermal melting and solidification process occurs.

3 Experimental Setup

Amorphous silicon films of 1.6 μm-thick were deposited on 0.525 mm-thick glass substrate using plasma enhanced chemical vapor deposition. The films were deposited at a rate of 60 Å/s in a hydrogen diluted silane environment at 380 °C with a hydrogen atomic concentration of around 20 at. %. Femtosecond laser texturing was carried out using a commercial Ti:sapphire oscillator and regenerative amplifier system. The system delivered 130-fs pulses of linearly polarized light at a 1 kHz repetition rate, and a central wavelength of 800 nm.

The sample is mounted on a three-axis translation stage and irradiated by laser pulses focused by a 60 mm focal-length lens. When changing the environment to water, the sample is placed in a plastic container, and the laser beam focused by the same lens travels through 5 mm of distilled water before striking the sample surface. The focal plane of the laser is moved below the sample surface in order to adjust the beam spot size. For both air and water cases the beam spot on the sample surface was circular with a diameter of 150 μm. The spikes generated at different fluences in water have a similar geometry, which suggests that they will have similar absorptance. Therefore, a fluence of 1.2 J/cm^2 is selected to produce typical results for underwater treatment. In order to reproduce the surface morphology observed for stationary processing at a fluence of 0.4 J/cm^2 with 100 pulses in air and at a fluence of 1.2 J/cm^2 with 50 pulses in water, 10×15 mm^2 areas were processed at specific scan speeds. The scan speed, v, is set by the Full width at half maximum (FWHM) of the Gaussian beam profile, d, the number of pulses, N, and the repetition rate of the laser, f, through the relation $v = df/N$ [23].

The untreated and treated samples were also observed through SEM. Surface roughness and the distribution of spikes in the treated samples were examined using an AFM. The optical transmittance and reflectance of both untreated and treated samples were measured by a spectrophotometer over a wavelength range of 250 nm–2500 nm which corresponds to the main spectral range of solar irradiation [24]. The reflectance (R in %) and transmittance (T in %) are then used to calculate the absorptance (A in %) of the film: $A = 100 - R - T$. X-ray diffraction (Cu K_α-line) was used for crystallinity estimation. X-ray photoelectron spectroscopy (XPS) is used for composition analysis.

4 Results and Discussion

4.1 Surface Morphology After Laser Scanning. When observed optically, the surface of the processed a-Si:H film is much darker than the original shiny reddish gray color which

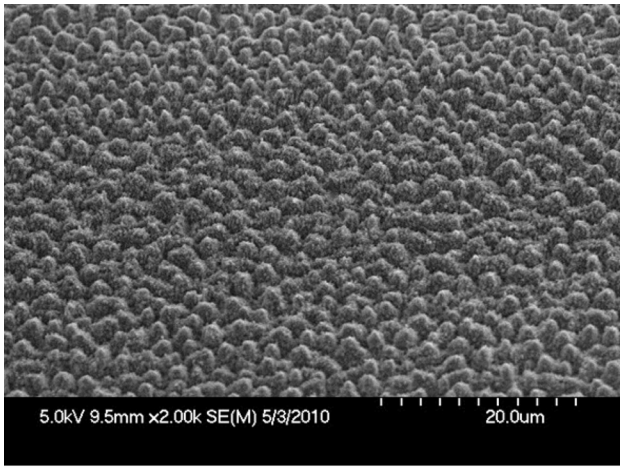

(*a*)

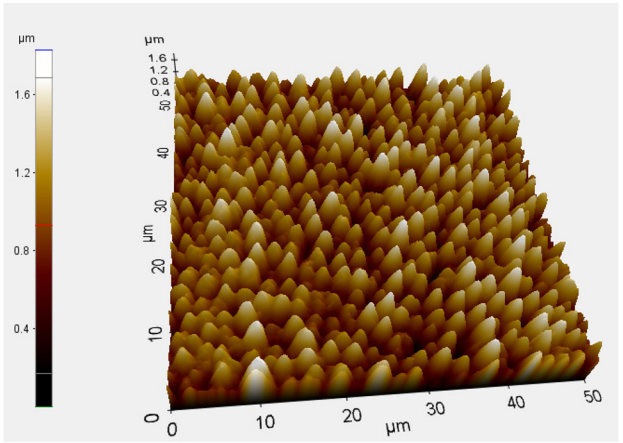

(*b*)

Fig. 1 (*a*) SEM image and (*b*) AFM image of surface of a-Si:H film laser irradiated in air (0.4 J/cm^2, 1 mm/s), showing texturing with conical spikes on the surface

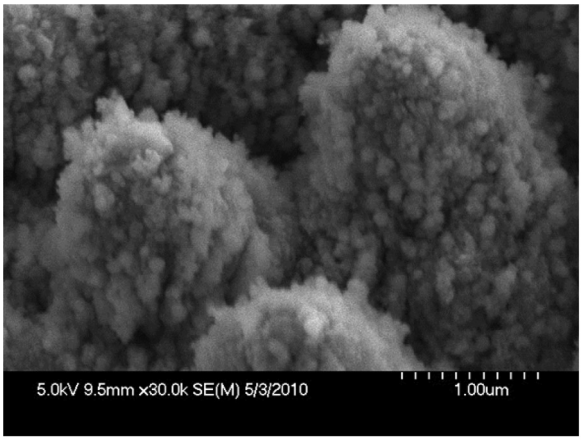

(*a*)

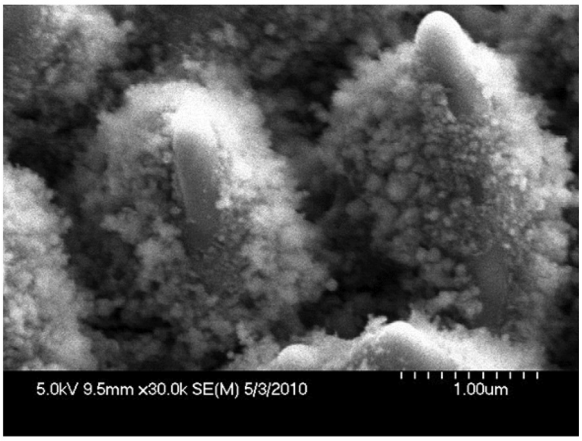

(*b*)

Fig. 2 Comparison of textured spikes made by (*a*) scanning (0.4 J/cm^2, 1 mm/s) and (*b*) stationary (0.4 J/cm^2, 100 pulses) pulsing in air, showing nanoparticles distributed on the whole spike after laser scanning

shows that the textured surface has the capability to trap light which greatly reduced the visible light reflection. Since the relationship of the formation of the spikes and number of pulses under different laser fluences is investigated in the previous studies [14–16], typical conditions, 0.4 J/cm^2 and 1.2 J/cm^2 in air and water, respectively, are selected to study the surface morphology via laser scanning. Figure 1(*a*) shows the SEM images of the surface processed at a fluence of 0.4 J/cm^2 and a speed of 1 mm/s in air, and the spikes look similar to those formed during stationary spot irradiation [14,16]. The AFM measurement in Fig. 1(*b*) shows that conical spikes are formed on the sample surface with an average height of 0.922 ± 0.0487 μm and an average spike spacing of 1.886 ± 0.0824 μm where the variation represents standard deviation. Figures 2(*a*) and 2(*b*) show high magnification SEM images of scanned and stationary processed sample surfaces; there are two visible differences between these two samples. First, the spikes on the stationary sample have a smooth conical shape at the tips while those on the scanned sample look blunter and lack this smooth conical shape. Second, the scanned sample has a larger amount of nanoscale particles spread across the spike surfaces. The nanoscale particles on the scanned sample are made of redeposited material from the ejected plasma plume and can lead to light scattering. On a stationary sample, most of this debris lies away from the area where the surface morphology forms and deposits as a ring around the irradiation spot [25]. The conical tips at the a-Si:H surface can be caused by resolidified droplets of redeposited molten silicon. The droplets at the tips are flowing around the spike surface toward the bottom due to gravity and a conical tip is formed after resolidification.

Figure 3 shows the SEM images of both a scanned sample surface treated at a fluence of 1.2 J/cm^2 at 2 mm/s and a stationary sample treated at 1.2 J/cm^2 at 50 pulses in water and similar spike formations are observed. The reason is that water convection and the motion of decomposed bubbles contribute to the reduction of debris redeposition. Therefore, the spike surfaces in both samples are smooth. The average spike height and spacing of scanned sample measured by AFM are 391.75 ± 2.612 nm and 218.63 ± 3.867 nm, respectively, which are close to those measured on stationary samples [14]; the variation represents standard error.

In order to analyze the chemical constituent on the spike surfaces, XPS measurements are carried out for untreated and treated samples in air and water. The results are shown in Fig. 4 and Table 1. The XPS survey results in Fig. 4 have been shifted vertically and superposed for clarity. The concentration of oxygen increases to almost 50% after laser treatment in air, which indicates that the nanoparticles attached on the spikes are silicon oxide (SiO_x). The 10% increase in oxygen concentration after underwater treatment is considered to be caused by the existence of a thicker oxidation layer on the surface compared to the as-received a-Si:H films. The oxidization layer is not desirable for absorption because it is an isolator; however, due to the smaller refractive index than that of a-Si:H, the reflectivity of silicon oxide layer is smaller. Based on Nayak et al. [13], the oxygen concentration decreases to less than 10% at the depth of 30 nm after laser processing, therefore, compared to the film thickness,

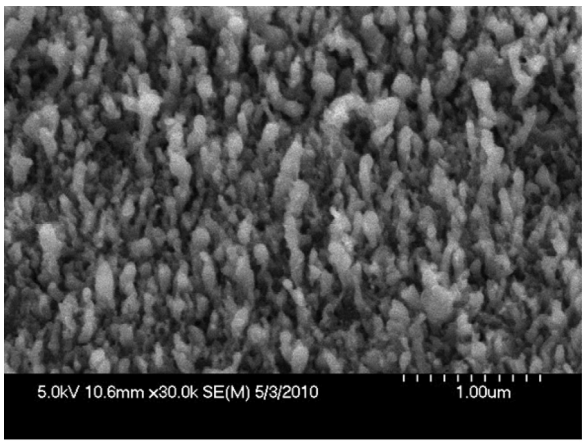

(*a*)

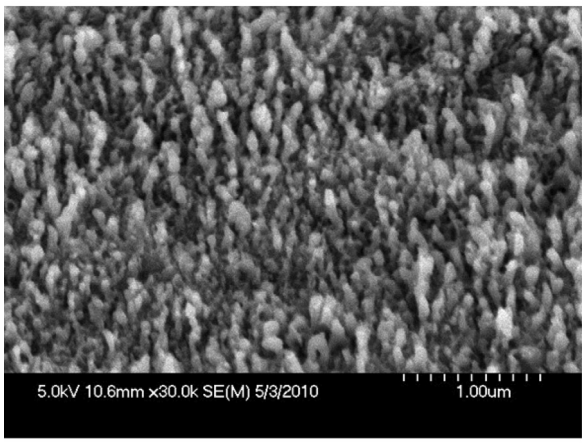

(*b*)

Fig. 3 Comparison of textured spikes made by (*a*) scanning (1.2 J/cm^2, 2 mm/s) and (*b*) stationary (1.2 J/cm^2, 50 pulses) pulsing in water, showing similar pillar-shaped spikes textured on the both sample surfaces

the oxidization layer is so thin that cannot affect the final absorption. The carbon peaks for both cases decrease almost to zero, this is due to the formation of carbon oxide (CO_x) during the processing, so that the solid-phase carbon changes to gas-phase carbon

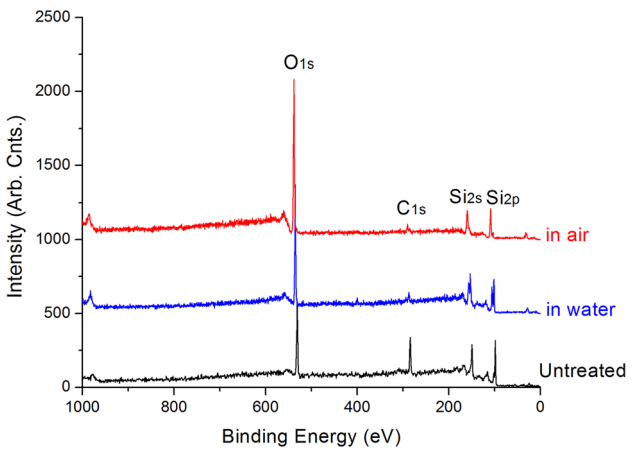

Fig. 4 XPS spectra of a-Si:H sample surfaces of as-received, laser irradiated in air (0.4 J/cm^2, 1 mm/s) and in water (1.2 J/cm^2, 2 mm/s). The spectra have been shifted up for clarity. Note increase in oxygen and decrease in carbon after laser processing.

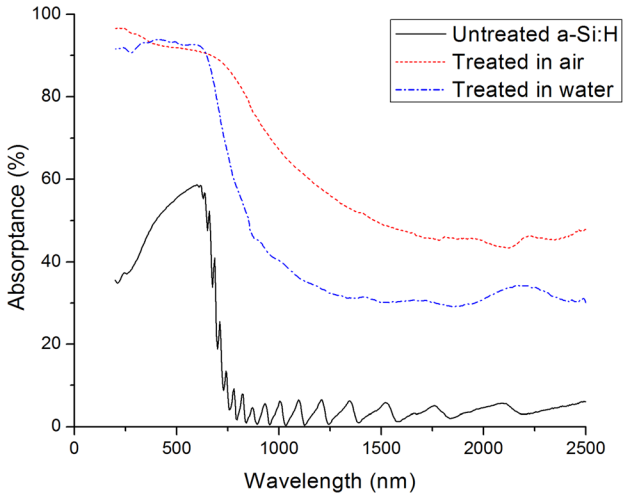

Fig. 5 Comparison of absorptance spectra of as-received and laser treated a-Si:H films at fluences of 0.4 J/cm^2 (scan speed 1 mm/s) and 1.2 J/cm^2 (scan speed 2 mm/s) in air and water by spectrophotometry, showing increase in absorptance over entire spectrum for both treated samples

oxide and is released into the air environment or forms bubbles which are suspended in the water.

4.2 Effect of Laser Processing on Absorption. Based on the spike formation by laser scanning, an area of 10 × 15 mm^2 is treated in order to investigate the effect of morphology change on absorption. Figure 5 shows the comparison of absorptance measurements of untreated and treated samples with surface texture consisting of low-density conical spikes formed in air and high-density pillar-shaped spikes formed in water. A dramatic increase in the absorptance can be seen for the treated a-Si:H films over the entire spectrum. The absorptance spectra for both treated samples go up to more than 90% from UV wavelengths to the bandgap of a-Si:H (730 nm) due to multiple reflections enabled by the surface texture, and decrease to around 45% and 30% in the below-bandgap region, for the air and water treated samples, respectively. The laser-induced oxidization layer can be also helpful for absorption enhancement, because it causes a reflection decrease at the surface due to the refractive index change. In the above-bandgap range, the absorptions for the samples processed under different conditions as a function of wavelength show different trends. The increase in absorptance for the untreated sample from UV wavelengths to the bandgap is mainly caused by the material's optical properties, which indicates that the absorption coefficient increases with increasing wavelength. However, the opposite trend is observed in the sample treated in air which may be caused by light scattering by the nanoparticles attached to the surface of the conical spikes (Fig. 2). According to Rayleigh scattering theory, when the radius of the particle is much smaller than the wavelength of the incident light, the intensity of scattered light is inversely proportional to the fourth power of the wavelength [26]

$$I(\lambda)_{\text{scattering}} \propto \frac{I(\lambda)_{\text{incident}}}{\lambda^4} \tag{3}$$

Table 1 Chemical constituent concentrations of the a-Si:H sample surfaces for as-received, laser irradiated in air and laser irradiated in water

Samples \ Elements	O_{1s} (%)	C_{1s} (%)	Si_{2s} (%)	Si_{2p} (%)
Untreated a-Si:H	22.1	23.6	21.6	32.6
Treated in water	32.01	3.44	31.26	33.29
Treated in air	47.4	4.28	22.86	25.46

where I and λ are intensity and wavelength, respectively. Therefore, at shorter wavelengths, a larger fraction of the incident light is scattered by the nanoparticles, which causes the highest absorptance to occur at the shortest wavelength. The absorptance spectrum of the sample treated in water is almost flat, which can be caused by much fewer nanoparticles being generated on the spikes due to the influence of water, thus a smaller fraction of light is scattered.

The differences in the below-bandgap absorptance of the treated a-Si:H samples could be attributed to different levels of crystallinity (bandgap of nc-Si:H is 1.1 eV) [27] which broadens the absorption range to 1100 nm while the textured surface introduces light trapping through multiple reflections as well as scattering by the nanoparticles. Moreover, the water environment may introduce less impurities and defects during processing which can cause fewer sub-bandgaps to form, which causes the material to absorb a smaller fraction of light with longer wavelengths compared to the sample treated in air. The reason why the absorptance starts decreasing at 730 nm rather than 1100 nm is due to the material remaining primarily amorphous with a bandgap of 730 nm. In the below-bandgap range, unlike for untreated a-Si:H, the absorptance curves for the treated films do not oscillate. The multiple reflections caused by the textured surface change the transmitted light paths through the film such that rays are not reflected back along their original paths, eliminating internal interference.

Overall, it is shown that the absorption can depend on the surface geometry, such as spike shape, density and attached nanoparticles, as well as crystallinity and impurity concentrations.

4.3 Modeling of Surface Geometry Effect on Absorption. In order to analyze the effect of surface geometry, a ray-tracing method [19,28] is used for calculating the path of waves through a system with regions of varying propagation velocity and absorption characteristics, based on geometrical optics. A solution is achieved by repeatedly advancing idealized narrow beams called rays through a medium by discrete amounts. A given ray is specified at a point, $\overline{P_0}$, as shown in Fig. 6, in a reference coordinate system $(\overline{X},\overline{Y},\overline{Z})$ with origin $\overline{O}(\overline{x_0},\overline{y_0},\overline{z_0})$, and has a certain wavelength, intensity and a direction of travel, $(\overline{k},\overline{l},\overline{m})$. An absorbing material with a surface, S, that is specified by an equation $F(X,Y,Z)=0$ is defined in coordinate system (X,Y,Z) having its origin at point O.

The first step is to transform the ray coordinates and direction cosine into their values in the (X,Y,Z) coordinate system. If the rotation angles between the (X,Y,Z) system and the $(\overline{X},\overline{Y},\overline{Z})$ system are (α,β,γ), the transformation matrix can be written as [28]

$$Q=\begin{bmatrix}(\cos\alpha\cos\gamma+\sin\alpha\sin\beta\sin\gamma) & -\cos\beta\sin\gamma & (-\sin\alpha\cos\gamma+\cos\alpha\sin\beta\sin\gamma)\\ (\cos\alpha\sin\gamma-\sin\alpha\sin\beta\cos\gamma) & \cos\beta\cos\gamma & (-\sin\alpha\sin\gamma+\cos\alpha\sin\beta\cos\gamma)\\ \sin\alpha\cos\beta & \sin\beta & \cos\alpha\cos\beta\end{bmatrix} \tag{4}$$

If $\overline{P_0}$ in coordinate (X,Y,Z) is $(\overline{X_0},\overline{Y_0},\overline{Z_0})$, the transformation equations for $\overline{P_0}$ and the ray direction vector are

$$\begin{bmatrix}X_0\\Y_0\\Z_0\end{bmatrix}=Q\begin{bmatrix}\overline{X_0}-\overline{x_0}\\\overline{Y_0}-\overline{y_0}\\\overline{Z_0}-\overline{z_0}\end{bmatrix}\text{ and }\begin{bmatrix}k\\l\\m\end{bmatrix}=Q\begin{bmatrix}\overline{k}\\\overline{l}\\\overline{m}\end{bmatrix} \tag{5}$$

Second, the point of intersection of the ray with the surface S is found. The parametric equations of the given ray may be written as [28]

$$X=X_0+ks,\quad Y=Y_0+ls,\quad Z=Z_0+ms \tag{6}$$

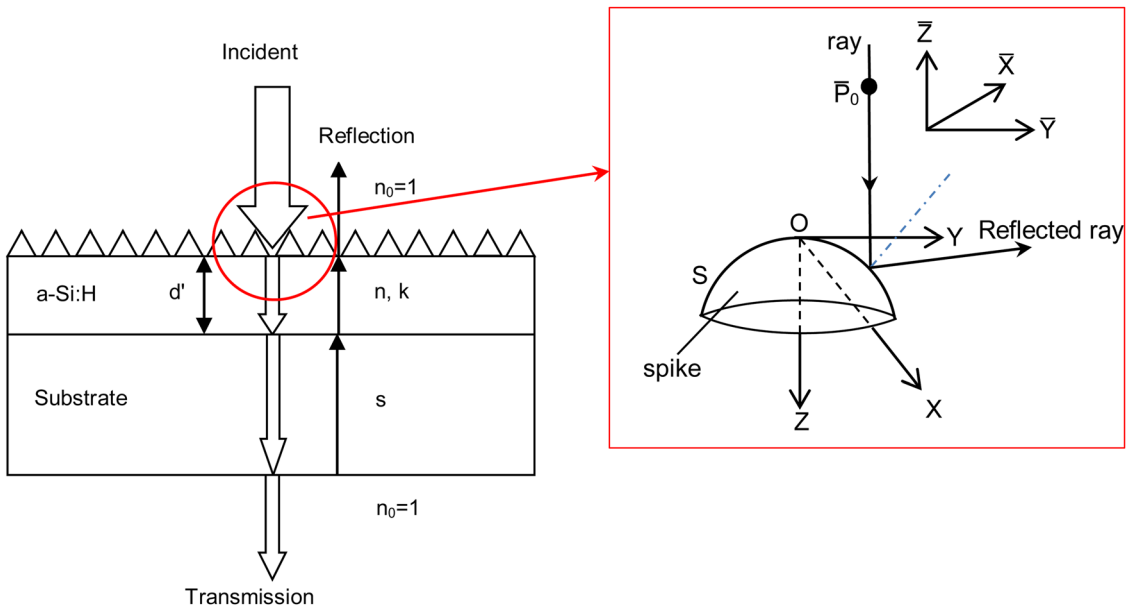

Fig. 6 Schematic of cross-sectional absorption simulation model for textured a-Si:H film on glass substrate, total thickness is 1.6 μm, real and imaginary parts of refractive index of a-Si:H film are *n* and *k*, *s* and n_0 are the refractive index of the substrate and air, respectively. Magnified image in the right shows the reference and local coordinate systems $(\overline{X},\overline{Y},\overline{Z})$ and (*X*, *Y*, *Z*), where *S* denotes the spike surface that reflects the ray passing through point $\overline{P_0}$

where s is the distance along the ray measured from (X_0, Y_0, Z_0). s is determined by satisfying the equation $F(X,Y,Z) = 0$, which can be calculated by a numerical method such as the Newton–Raphson iteration technique as follows [28]

$$s_{j+1} = s_j - F(X_j, Y_j, Z_j)/F'(X_j, Y_j, Z_j) \tag{7}$$

where, $X_j = X_0 + ks_j$, $Y_j = Y_0 + ls_j$, $Z_j = Z_0 + ms_j$, and

$$F'(X_j, Y_j, Z_j) = dF/ds(s = s_j) = \frac{\partial F}{\partial X_j}k + \frac{\partial F}{\partial Y_j}l + \frac{\partial F}{\partial Z_j}m \tag{8}$$

This process starts from the first approximation, $s_1 = 0$, and is terminated with the value s_f for which $|s_f - s_{f-1}| < \varepsilon$, where ε is a small pre-assigned tolerance.

Third, the change in direction at the intersection point of the ray and the surface is found. Reflection is based on Snell's law and the intensity change is determined by Fresnel's equations.

Fourth, the second and third steps are repeated to find the subsequent points of intersection of the reflected ray with the surface, and the absorption caused by the ray traveling through the material is calculated based on Beer Lambert's law, until the intensity of the ray decreases to a negligible amount, e.g., 0.1% of the original intensity. The absorptance, $A(\lambda,i)$, reflectance, $R(\lambda,i)$, and transmittance, $T(\lambda,i)$ of a given ray i at wavelength λ are the total absorbed, reflected, and transmitted intensities, respectively, divided by the initial ray intensity $I(\lambda,i)$.

Lastly, if the light source is defined by a spectrum from λ_1 to λ_2, and for each wavelength it can be divided into a discrete number of rays, p, at different initial points $\overline{P_0}$ and propagation directions $(\overline{k}, \overline{l}, \overline{m})$, the relationship between absorptance, reflectance, transmittance, and source intensity can be described as

$$\sum_{\lambda_1}^{\lambda_2}\sum_{i=1}^{i=p}[A(\lambda,i) + R(\lambda,i) + T(\lambda,i)]I(\lambda,i) = I_{\text{lightsource}} \tag{9}$$

In this paper, the model is realized by a ray-tracing software TRACEPRO [19]. The Monte Carlo method is used to sample the distribution of rays emanating from light sources and each ray with a certain intensity, direction and wavelength is traced through the model structure. Consequently, portions of the ray are reflected or refracted at every interface and absorbed through the film, with the fraction being calculated by the angle of incidence and the optical properties. The model configuration consisting of an a-Si:H thin film on a glass substrate is shown in Fig. 6. Since the absorption coefficient of crystalline silicon is 2 orders of magnitude less than that of a-Si:H, and the amount of crystalline silicon after crystallization is much smaller than that of a-Si:H, the model does not consider the effect of crystallization on the thin film absorptance. The model also assumes that the entire structure is uniform and no nanoparticles are attached on the spikes; therefore internal defects and Rayleigh scattering are not simulated. The surface structures are designed with dimensions similar to the conical and pillar-shaped spikes formed in air and water, respectively. The simulated area is 300 × 300 μm^2, and the diameter of the circular light source is 200 μm with a wavelength range between 250 nm and 2500 nm. The wavelength step is 10 nm, and a set of 60,000 rays are randomly generated with a total intensity of 1 W. The light is normally incident to the textured surface with conical spikes, and has a 45 deg incident angle to the surface with pillar-shaped spikes.

Figures 7 and 8 show the comparison between the simulated and measured absorptance spectra of the samples treated in air and water, respectively. The overall trends of the simulation curves are similar to the measurement spectra except in the above-bandgap range. All of the simulated results show a similar trend to the untreated sample in this wavelength range (Fig. 5), which suggests that the difference is neglect of the Rayleigh scattering effect by the nanoparticles as discussed above. The underestimate in the below-bandgap region can be caused by neglecting the scattering effect. Moreover, ignoring the crystallization effect, defects, and impurities generated after laser processing could be another reason of underprediction. As known, the defects can act as recombination centers for electron-hole pairs, and the impurities may introduce sub-bandgaps that absorb light with longer wavelengths. Furthermore, the simplification of periodic surface structure in the model differs from the exact spikes generated after laser processing, especially since the pillar-shaped spikes formed in water are pointed in different directions and are more irregular than the simulated model geometry. Therefore, the real spike shape and distribution can obtain a greater number of reflections at the surface than the regular pillar-shaped surface simulation, which causes underestimation of the absorptance over the entire spectrum. However, most of the characteristics of the measurement are captured by the simulated curves, so that the model can be used for estimating the effect of different surface geometries on the absorptance. During the comparison, it can be seen that the conical spikes have better absorption performance than pillar-shape spikes.

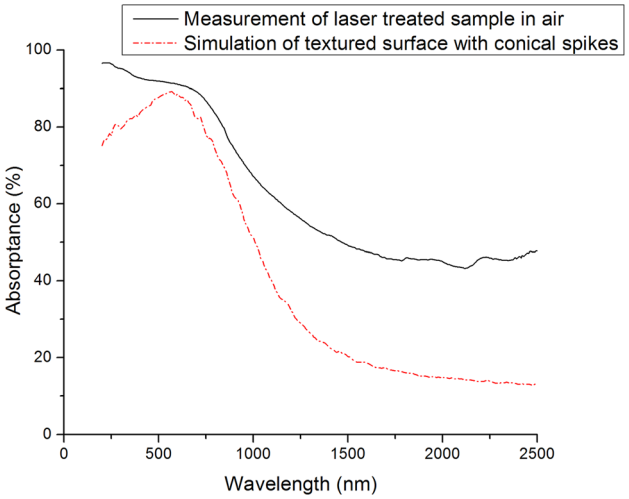

Fig. 7 Comparison of simulated and measured absorptance spectra of the laser treated sample in air with the textured surface of conical spikes, with height of 900 nm and top angle of 90 deg

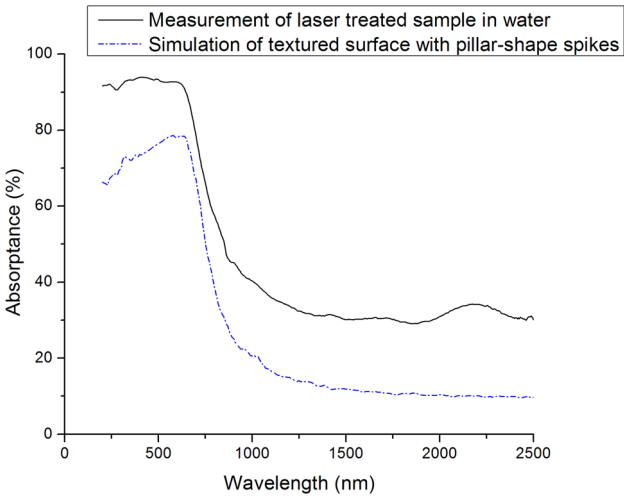

Fig. 8 Comparison of simulated and measured absorptance spectra of the laser treated samples in water with textured surface of pillar-shaped spikes with height of 400 nm height and a diameter of 100 nm

In order to further understand the effect of different geometric factors, two models with different spike densities and heights are investigated. Figure 9 shows the simulated absorptance spectra of textured surfaces with conical spikes of different densities. The inset image shows the schematic of the spike distribution on the surface. It is assumed that the spike geometric parameters, such as height (900 nm) and top angle (90 deg), are the same, and the only difference is the density, one is 4 times as the other. During the spike formation process, when the surface shows a bead-like structure as seeds of the spikes, the average bead spacing, which is similar to the final average spike spacing, is different under different fluences. And then using different number of pulses under those fluence conditions can generate similar geometries of the spikes with different distances between the adjacent spike bases. In order to simplify the problem, it is treated as a flat area in between the spike bases during the simulation.

The results indicate that the surface with higher density spikes has better absorption performance. This is because the sample with higher density has less open space in between the spike bases, which cannot cause multiple reflections. The reflectance on a unit surface with higher density spikes will be much less so that the absorptance is higher. However, in the below-bandgap region, the absorption performance deteriorates when the wavelength increases. The light with longer wavelength is more difficult to be absorbed due to the low photon energy, although the multiple reflections still occur. This can also explain why the difference between the absorptance spectra becomes smaller and smaller. According to the better absorption performance by the surface with high-density conical spikes, it can be seen that the factor of spike shape plays a more important role in absorption. The simulated absorptance spectra of textured surfaces with different height of conical spikes are shown in Fig. 10, and the inset image shows the schematic of the spike distribution on the surface. It is assumed that the spikes are closed-packed (spikes are connected together) and the shape and top angle are the same, and one sample has a twice height texturing as the other. It shows that the absorptance performances for different height spikes are almost the same. The reason is that for those closed-packed spikes with the same top angle, no matter how the spike height and density are, the number of times a ray is reflected between spikes is the same, so that the distance traveled by the rays inside the two samples are very similar, and the total absorptance is similar.

4.4 Effect of Laser Processing on Crystallinity. In order to study the crystallization of the treated films, X-ray diffraction patterns were taken for the untreated and treated a-Si:H films in air and water and are shown in Fig. 11. The spectra have been shifted vertically for clarity. All the spectra show an amorphous peak around $2\theta = 25$ deg, which is caused by the internal constructive interference of the amorphous Si network. Three peaks at around $2\theta = 29$ deg, 47 deg, and 56 deg emerge after processing in air which indicate a structural change after laser irradiation and can be indexed to the (111), (220), and (311) crystalline orientations of silicon. During femtosecond laser processing an ultrafast nonthermal disorder-to-disorder phase transition occurs within a few picoseconds of the laser pulse which cannot lead to crystallization. The material is then partially melted due to thermal diffusion after energy transfer from the excited electrons to the material. The resolidification of the melted layer proceeds via vertical growth from the remaining unmelted material and results in random crystal orientations due to the amorphous structure of the film. According to the silicon powder diffraction file, the highest three intensities of X-ray diffraction are for the (111), (220), and (311) orientations and are the same as observed in Fig. 11. The crystallization is considered to be under the partial melting regime, resulting in no preferential orientation during solidification. This

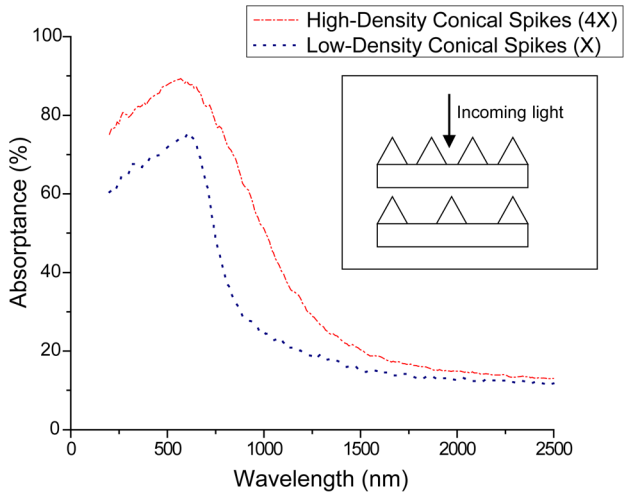

Fig. 9 Comparison of simulated absorptance spectra for the textured surfaces with two different densities of conical spikes, showing the surface with higher density spikes has higher absorptance

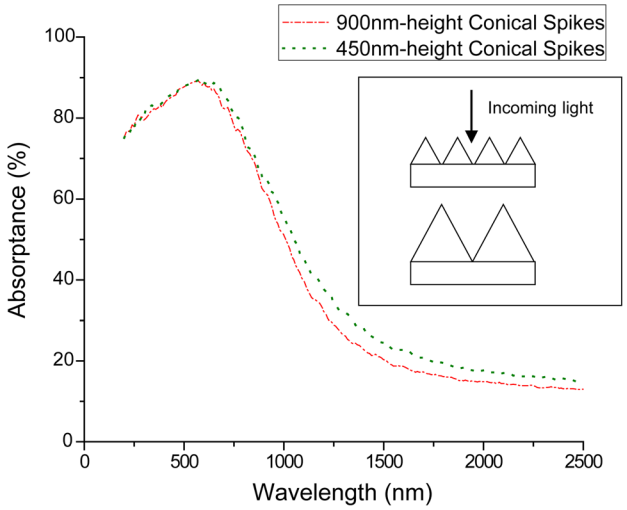

Fig. 10 Comparison of simulated absorptance spectra for textured surfaces with different heights of conical spikes, showing similar absorptance over the entire wavelength range

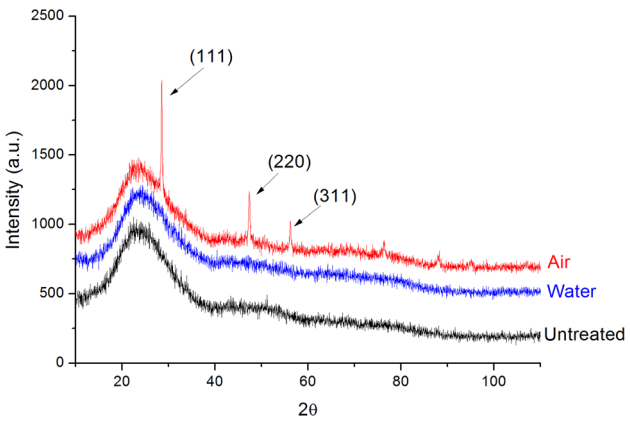

Fig. 11 X-ray diffraction spectra of as-received a-Si:H film, laser treated films at 0.4 J/cm^2, 1 mm/s and 1.2 J/cm^2, 2 mm/s in air and water, respectively. All the spectra show an "amorphous peak" at around $2\theta = 25$ deg and no signs of crystallinity for the untreated sample and that treated in water. Sample treated in air shows three different peaks for (111), (220), and (311) orientation of silicon. The spectra have been shifted for clarity.

suggests that the laser irradiated film becomes a mixture of nc-Si:H and a-Si:H with most of the nc-Si:H believed to be contained within the top melted surface. However, the XRD pattern also shows that the sample treated in water at 1.2 J/cm^2 with a scan speed of 2 mm/s has no crystallinity.

In order to further understand the laser processing parameters, fluence and scan speed, effect on crystallinity in water, a film was treated with a lower fluence (0.5 J/cm^2) at 2 mm/s and at a higher scan speed (25 mm/s). The XRD patterns are shown in Fig. 12. Only the sample treated at 0.5 J/cm^2 with scan speed of 25 mm/s has two small peaks that can be indexed to the (111) and (220) orientations of silicon. The reason is due to the higher cooling rate in a water environment than in air; the melted silicon resolidifies so quickly that much less material is able to crystallize. The sample processed at the same fluence, 0.5 J/cm^2, but lower scan speed of 2 mm/s has no crystallinity; the reason could be the higher pulse overlap during processing. Daminelli et al. [29] showed that the ablation threshold of silicon decreases with increasing number of pulses due to modification of the absorption behavior of the film such that subsequent surface texturing occurs at fluence levels lower than for previous pulses. Processing with this decreased threshold caused by higher overlap can be considered to be equivalent to processing at a higher fluence and lower overlap. The femtosecond laser-induced crystallization is ablation-dominant process rather than that of nanosecond laser which crystallinity is proportional to the laser energy since it is a melting-dominant process. Therefore, more material will be removed by a higher energy input, resulting in a deeper buried melting thin layer underneath. This deeper melting layer will cause larger temperature gradients through thickness direction compared to that of lower energy input. Therefore, a higher cooling rate is induced during the solidification process and the liquid layer does not have enough time to be crystallized. Similarly, Fig. 13 shows the XRD pattern of samples treated at the same scan speed, 25 mm/s, but different fluences from 0.5 to 0.8 J/cm^2. It can be seen that the crystallinity decreases with increasing fluence, and fluences larger than 0.7 J/cm^2 do not introduce crystallinity. The femtosecond laser-induced crystallization has a nonthermal melting process within 1 about picosecond; however, it will not affect the crystallization. The crystallization happened at nanosecond scale when the energy transferred back from free electrons to material and started melting the material. Therefore, Eq. (1) is no longer valid for analyzing the temperature distribution at this point. It is assumed that the process can be separated by two models—nonlinear absorption (free electron excitation) and linear thermal diffusion (energy

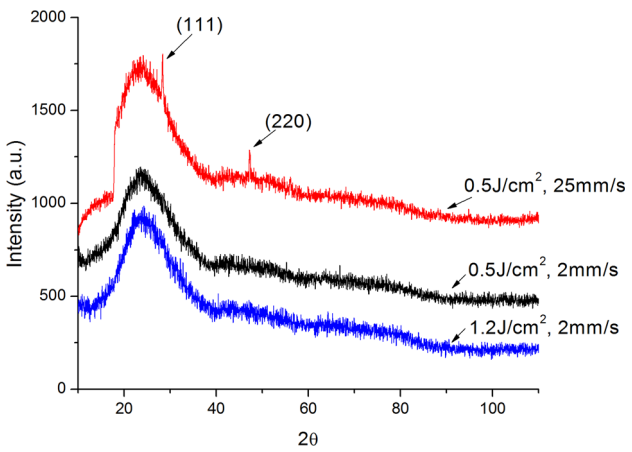

Fig. 12 X-ray diffraction spectra of a-Si:H films laser treated at fluences of 0.5 J/cm^2 and 1.2 J/cm^2, and scan speeds of 2 mm/s and 25 mm/s in water. An "amorphous peak" around $2\theta = 25$ deg is observed for all samples. Sample processed at 0.5 J/cm^2 and 25 mm/s shows existence of two peaks for (111) and (220) orientation of silicon, showing the effect of different laser parameters on crystallinity

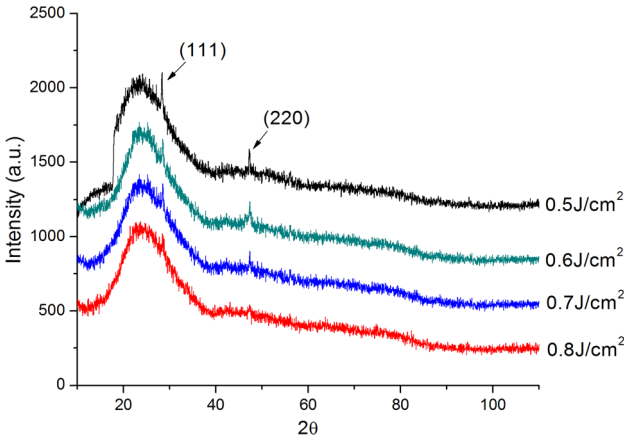

Fig. 13 X-ray diffraction spectrum of laser treated a-Si:H film at different fluences from 0.5 J/cm^2 to 0.8 J/cm^2 with the same scan speed of 25 mm/s in water. An "amorphous peak" around $2\theta = 25$ deg is observed for all samples. Existence of two overall different peaks for (111) and (220) orientation of silicon is found except for the condition at 0.8 J/cm^2, showing that the crystallinity decreases with increasing of fluence.

transferred back to material). Therefore, for the crystallization process, it can be assumed that the heat source is from those free electrons rather than the laser and the energy loss during the electron movement is negligible. The thermal effects of laser processing on crystallization can be described using a model that is based on one-dimensional heat flow given by [30]

$$c_s(T)\rho_s(T)\frac{\partial T(x,t)}{\partial t} = \frac{\partial}{\partial x}\left[\kappa(T)\frac{\partial T(x,t)}{\partial x}\right] + S(x,t) \tag{10}$$

where $T(x,t)$ is the temperature distribution, $c_s(T)$ is the specific heat, $\rho_s(T)$ is the density, $\kappa(T)$ is the thermal conductivity, and $S(x,t)$ is the source which is proportional to the energy absorbed by the surface layer estimated by

$$S(x,t) = \alpha(t)I(x,t) \quad \text{and} \quad I(x,t) = I_0(t)[1 - R(T)]e^{-\alpha(T)x} \tag{11}$$

where $R(T)$ is the reflectivity, $\alpha(t)$ is absorption coefficient, and $I_0(t)$ is the intensity that absorbed by free electrons which is proportional to the laser pulse intensity.

As discussed in Sec. 2.2, thermal melting occurs underneath the ablated layer and is caused by thermal diffusion, thus the higher the fluence, the thicker the ablated layer, and the deeper the thermally melted layer will be. Based on Eq. (10), the influence of laser fluence on the temperature distribution along the depth of the film is shown in Ref. [30]; it can be seen that the temperature gradient increases with increasing fluence and depth into the film. Thus, the thermal melting caused by higher fluences introduces steeper temperature gradients compared to lower fluence treated samples and can be solidified quicker. Thus, the higher fluence can cause a higher cooling rate, which accelerates the cooling/resolidification process and reduces crystallinity.

4.5 Effect of Crystallinity on Absorption. Figure 14(*a*) shows an SEM image of an a-Si:H film surface laser treated at a fluence of 0.5 J/cm^2 with a scan speed of 25 mm/s in water. The small nanosize spikes with blunt tips are randomly orientated and irregularly distributed on the surface after laser treatment. The surface roughness and spike distribution is further observed in the AFM image in Fig. 14(*b*), which shows an average spike height of 138 ± 2.58 nm and an average spike spacing of 216 ± 6.77 nm where the variation represents standard error. Visually, the surface texture is similar to that of samples treated at a higher fluence of 1.2 J/cm^2 at a scan speed of 2 mm/s (Fig. 3), moreover, the spike

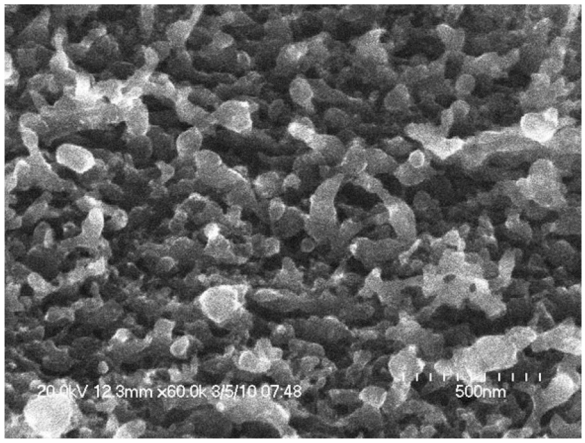

(*a*)

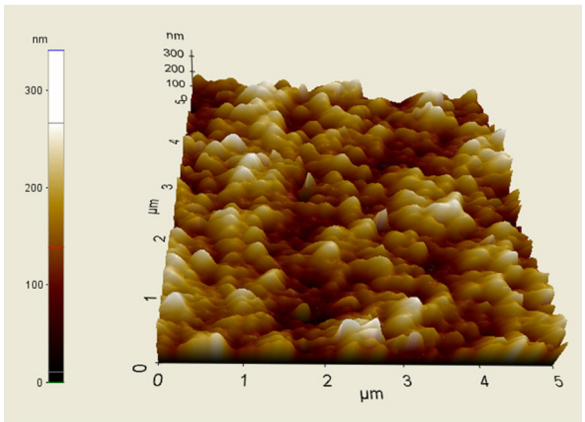

(*b*)

Fig. 14 (*a*) SEM image and (*b*) AFM image of surface of a-Si:H film laser irradiated in water (0.5 J/cm^2, 25 mm/s), showing texturing with randomly oriented spikes on the surface

spacing measured through AFM of the two samples are also close, and spike heights are 138 nm and 391 nm, respectively. Therefore, the absorptance of these two samples should be similar if both are not crystallized, since the spike height does not affect the result as discussed above. In fact, the sample processed at 25 mm/s is partially crystalline while the sample processed at 2 mm/s is not. The comparison of these two samples can show the effect of crystallization on absorption. Figure 15 shows the absorptance versus wavelength for both the crystallized and noncrystallized samples, and the untreated sample is also included for comparison. As seen, due to the similar surface texture, in the above-bandgap region, the absorptance spectra of both laser treated samples are almost the same, no matter how deep the spikes are. The change in crystallinity is not significant here since the majority of the material is still a-Si:H after processing. The highest absorptance from the bandgap to around 1600 nm is for the crystallized sample processed at 0.5 J/cm^2, followed by the noncrystallized sample treated at 1.2 J/cm^2; the reason could be that the crystallized portion of the sample has a bandgap of 1.1 eV, which helps to absorb light with wavelengths up to 1100 nm. Moreover, the crystallized sample has a thicker a-Si:H layer due to the formation of shorter spikes and the resulting higher defect and impurity concentrations could also cause higher absorption. The reason that the crystallized sample has lower absorption for wavelengths above 1600 nm is not well understood. However, based on the solar radiation spectrum, the radiation intensity in this range is a very small portion of the total intensity [24], which suggests that lower absorption at these higher wavelengths will only have a small effect on the total energy absorption. Therefore, over the entire range of the

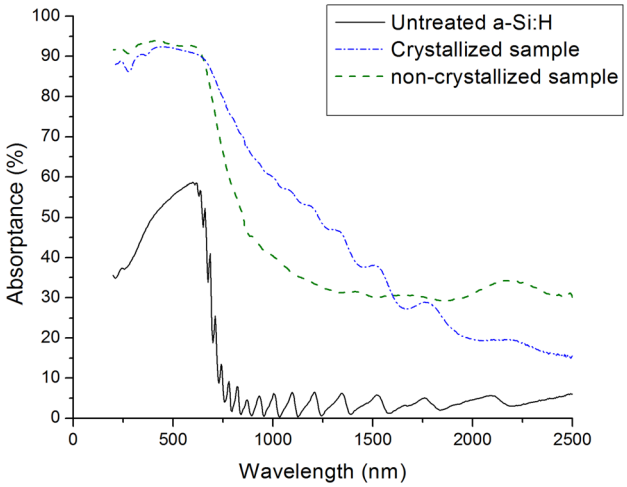

Fig. 15 Comparison of absorptance spectra measured by spectrophotometry of as-received and laser irradiated a-Si:H films with and without crystallinity at different fluences and scan speeds (0.5 J/cm^2 at 25 mm/s, 1.2 J/cm^2 at 2 mm/s) in water, showing the effect of crystallinity on absorption

spectrum, it can be concluded that with similar surface structure, a crystallized sample has better absorption performance due to the combination of both surface texturing and crystallization.

4.6 Effect of Processing Medium on Absorption. In order to compare the effect on different factors, such as surface geometry and crystallinity, absorptance spectra for samples treated in air (0.4 J/cm^2 and 1 mm/s) and in water (0.5 J/cm^2 and 25 mm/s) are shown in Fig. 16. It shows that the sample treated in air has better absorptance performance over the entire spectrum. In the above-bandgap region, the conical spikes and attached nanoparticles formed on the sample treated in air can induce greater light reflection and scattering between the spikes, which play a more important role in absorptance than spike density, which is higher for the water treated sample. The conical spikes, greater crystallinity, as well as the defects and impurities formed during the laser processing in air introduce greater numbers of reflections, a wider absorption spectrum, and sub-bandgaps for the sample treated in air. These effects all work to increase the absorptance in the below-bandgap region to

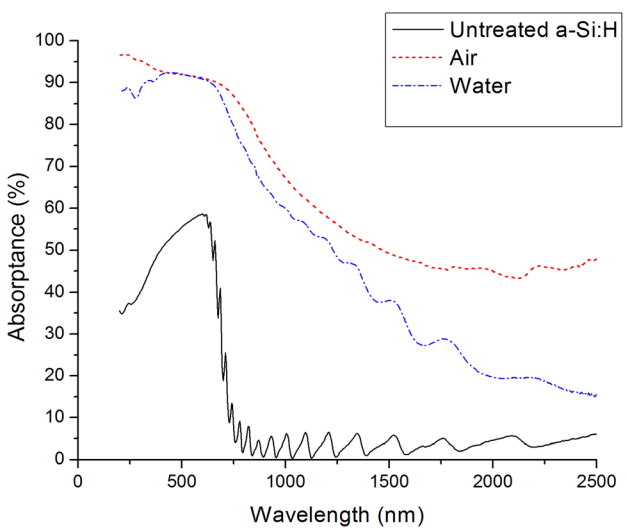

Fig. 16 Comparison of absorptance spectra measured by spectrophotometry of as-received and laser irradiated a-Si:H film in air (0.4 J/cm^2, 1 mm/s) and water (0.5 J/cm^2, 25 mm/s), showing the effect of different factors, such as surface geometry, crystallinity and processing medium on absorption

above that achieved by the sample treated in water. Therefore, with a sufficient thickness of a-Si:H left after laser processing for absorption, a treated sample surface having regular spike shapes with sharper angles, attached nanoparticles, more crystallinity, greater defect and impurity concentrations, and larger spike densities will have better absorptance. Compared to the absorptance spectra of the crystalline silicon wafers laser treated in different background gas environments as show by Younkin et al. [11], it can be seen that both textured crystalline bulk silicon and a-Si:H thin films in air have similar absorptance performance in the above-bandgap region. In the below-bandgap range, the absorptance of crystalline silicon drops quickly to almost zero, but for the a-Si:H film, the absorptance only drops to around 45% and remains more or less constant with increasing wavelength. Therefore, comparing the thicknesses of a few hundred microns for crystalline silicon and 1.6 μm for a-Si:H, it can be concluded that a-Si:H thin films have greater absorptance while being more economical than c-Si and may be ideal for solar cell fabrication.

5 Conclusion

In conclusion, it has been demonstrated that simultaneously improving the absorptance of sunlight and the stability against the SWE of a-Si:H thin films is possible through femtosecond laser irradiation in both air and water. Absorptance enhancement is caused by light trapping based on the surface geometry changes, as well as increased defect and impurity concentrations caused by laser processing. The change in crystallinity after processing reduces the thickness of the a-Si:H layer but may allow for greater stability in a-Si:H-based solar cells and broadens the absorptance range to 1100 nm. Furthermore, the correlation between the crystallinity, scan speed and fluence when treated in water have been investigated; the crystallinity decreases with increasing laser fluence and decreasing scan speed, which may be due to the increased cooling rate caused by the higher surface temperature and temperature gradient. Finally, the absorptance spectra indicate that the samples treated in air with regular conical spikes, crystallization and high defect and impurity concentration have the best absorption performance over the solar radiation spectrum. Compared with the absorptance of laser textured crystalline bulk silicon, it can be concluded that femtosecond laser processing of a-Si:H thin films may allow for more efficient and economical solar cell applications.

Acknowledgment

Research carried out in part at the Center for Functional Nanomaterials, Brookhaven National Laboratory, which is supported by the U.S. Department of Energy, Office of Basic Energy Sciences, under Contract No. DE-AC02-98CH10886. The use of material characterization equipment at Materials Research Science and Engineering Center, Columbia University is gratefully acknowledged. The authors also would like to thank Professor Vijay Modi, Department of Mechanical Engineering, Columbia University, for helpful discussion and suggestions.

References

[1] Luque, A., and Hegedus, S., 2003, *Handbook of Photovoltaic Science and Engineering*, Wiley, UK, Chap. 7-8.
[2] Chopra, K. L., Paulson, P. D., and Dutta, V., 2004, "Thin-Film Solar Cells: An Overview," Prog. Photovoltaics, **12**, pp. 69–92.
[3] Kazmerski, L. L., 2006, "Solar Photovoltaics R&D at the Tipping Point: A 2005 Technology Overview," J. Electron Spectrosc. Relat. Phenom., **150**, pp. 105–135.
[4] Miles, R. W., Hynes, K. M., and Forbes, I., 2005, "Photovoltaic Solar Cells: An Overview of State-of-the-Art Cell Development and Environmental Issues," Prog. Cryst. Growth Charact. of Mater., **51**, pp. 1–42.
[5] Staebler, D. L., and Wronski, C. R., 1980, "Optically Induced Conductivity Changes in Discharge-Produced Hydrogenated Amorphous Silicon," J. Appl. Phys., **51**(6),p. 3262.
[6] Kolodziej, A., 2004, "Staebler-Wronski Effect in Amorphous Silicon and Its Alloys," Opto-Electron. Rev., **12**(1), pp. 21–32.
[7] Yamamoto, K., Nakajima, A., Yoshimi, M., Sawada, T., Fukuda, S., Suezaki, T., Ichikawa, M., Koi, Y., Goto, M., Meguro, T., Matsuda, T., Kondo, M., Sasaki, T., and Tawada, Y., 2004, "A High Efficiency Thin Film Silicon Solar Cell and Module," Sol. Energy, **77**, pp. 939–949.
[8] Gosain, D. P., Machida, A., Fujino, T., Hitsuda, Y., Nakano, K., and Sato, J., 2003, "Formation of (100)-Textured Si Film Using an Excimer Laser on a Glass Substrate," Jpn. J. Appl. Phys., Part 2, **42**, pp. L135–L137.
[9] Shieh, J., Chen, Z., and Dai, B., 2004, "Near-Infrared Femtosecond Laser-Induced Crystallization of Amorphous Silicon," Appl. Phys. Lett., **85**(7), pp. 1232–1234.
[10] Choi, T. Y., Hwang, D. J., and Grigoropoulos, C. P., 2003, "Ultrafast Laser-Induced Crystallization of Amorphous Silicon Films," Opt. Eng., **42**(11), pp. 3383–3388.
[11] Younkin, R., Carey, J. E., Mazur, E., and Levinson, J. A., and Friend, C. M., 2003, "Infrared Absorption by Conical Silicon Microstructures Made in a Variety of Background Gases Using Femtosecond-Laser Pulses," J. Appl. Phys., **93**(5), pp. 2626–2629.
[12] Sheehy, M. A., Winston, L., Carey, J. E., Friend, C. M., and Mazur, E., 2005, "Role of the Background Gas in the Morphology and Optical Properties of Laser-Microstructured Silicon," Chem. Mater, **17**, pp. 3582–3586.
[13] Nayak, B. K., and Gupta, M. C., 2007, "Femtosecond-Laser-Induced-Crystallization and Simultaneous Formation of Light Trapping Microstructures in Thin a-Si:H Films," Appl. Phys. A, **89**, pp. 663–666.
[14] Wang, H., Kongsuwan, P., Satoh, G., and Yao, Y. L., "Femtosecond Laser-Induced Simultaneous Surface Texturing and Crystallization of a-Si:H Thin Film: Morphology Study," Int. J. Adv. Manuf. Technol. (in press).
[15] Wang, H., Kongsuwan, P., Satoh, G., and Yao, Y. L., 2011, "Effect of Processing Medium and Condition on Absorption Enhancement of Femtosecond Laser Treated a-Si:H Thin Film," *Proceedings of the 2011 North American Manufacturing Research*, Corvallis, OR.
[16] Wang, H., Kongsuwan, P., Satoh, G., and Yao, Y. L., 2010, "Femtosecond Laser-Induced Simultaneous Surface Texturing and Crystallization of a-Si:H Thin Film," *Proceedings of the 2010 International Manufacturing Science and Engineering Conference*, Erie, PA.
[17] Yagi, T., Uraoka, Y., and Fuyuki, T., 2006, "Ray-Trace Simulation of Light Trapping in Silicon Solar Cell With Texture Structures," Sol. Energy Mater. Sol. Cells, **90**, pp. 2647–2656.
[18] Halbwax, M., Sarnet, T., Delaporte, P., Sentis, M., Etienne, H., Torregrosa, F., Vervisch, V., Perichaud, I., and Martinuzzi, S., 2008, "Micro and Nanostructure of Silicon by Femtosecond Laser: Application to Silicon Photovoltaic Cells Fabrication," Thin Solid Films, **516**, pp. 6791–6795.
[19] Hua, X., Zhang, Y., and Wang, H., 2010, "The Effect of Texture Unit Shape on Silicon Surface on the Absorption Properties," Sol. Energy Mater. Sol. Cells, **94**, pp. 258–262.
[20] Vechten, J. A., Tsu, R., and Saris, F. W., 1979, "Nonthermal Pulsed Laser Annealing of Si; Plasma Annealing," Phys. Lett. A, **74**(6), pp. 422–426.
[21] Linde, D., and Fabricius, N., 1982, "Observation of an Electronic Plasma in Picosecond Laser Annealing of Silicon," Appl. Phys. Lett., **41**(10), pp. 991–993.
[22] Callan, J. P., Kim, A, Roeser, C. A. D., Mazur, E., Solis, J., and Siegel, J., Afonso, C. N., 2001, "Ultrafast Laser-Induced Phase Transitions in Amorphous GeSb Films," Phys. Rev. Lett., **86**(16), pp. 3650–3653.
[23] Crouch, C. H., Carey, J. E., Shen, M., Mazur, E., and Fenin, F. Y., 2004, "Infrared Absorption by Sulfur-Doped Silicon Formed by Femtosecond Laser Irradiation," Appl. Phys. A, **79**, pp. 1635–1641.
[24] Goetzberger, A., Knobloch, J., and Voss, B., 1998, *Crystalline Silicon Solar Cells*, Wiley, Chichester, Chap. 2.
[25] Carey, J. E., 2004, "Femtosecond-Laser Microstructuring of Silicon for Novel Optoelectronic Devices," Ph.D. dissertation, Harvard University, Cambridge, MA.
[26] Steen, W., 2003, *Laser Material Processing*, 3rd ed., Springer-Verkag, London, pp. 76–77.
[27] Meillaud, F., Feltrin, A., Dominé, D., Buehlmann, P., Python, M., Bugnon, G., Billet, A., Parascandolo, G., Bailat, J., Fay, S., Wyrsch, N., Ballif, C., and Shah, A., 2009, "Limiting Factors in the Fabrication of Microcrystalline Silicon Solar Cells and Microcrystalline/Amorphous ('Micromorph') Tandems," Philos. Mag., **89**(28), pp. 2599–2621.
[28] Spencer, C. H., and Murty, M. V. R. K., 1962, "General Ray-Tracing Procedure," J. Opt. Soc. Am., **52**(6), pp. 672–678.
[29] Daminelli, G., Kruger, J., and Kautek, W., 2004, "Femtosecond Laser Interaction With Silicon Under Water Confinement," Thin Solid Films, **467**, pp. 334–341.
[30] Palani, I. A., Vasa, N. J., and Singaperumal, M., 2008, "Crystallization and Ablation in Annealing of Amorphous-Si Thin Film on Glass and Crystalline-Si Substrates Irradiated by Third Harmonics of Nd^{3+}: YAG Laser," Mater. Sci. Semicond. Process., **11**, pp. 107–116.